



CHORUS

This is the accepted manuscript made available via CHORUS. The article has been published as:

Dimensionality-Induced Change in Topological Order in Multiferroic Oxide Superlattices

Megan E. Holtz, Elliot S. Padgett, Rachel Steinhardt, Charles M. Brooks, Dennis Meier,
Darrell G. Schlom, David A. Muller, and Julia A. Mundy

Phys. Rev. Lett. **126**, 157601 — Published 12 April 2021

DOI: [10.1103/PhysRevLett.126.157601](https://doi.org/10.1103/PhysRevLett.126.157601)

Dimensionality-induced change in topological order in multiferroic oxide superlattices

Megan E. Holtz^{1,2}, Elliot S. Padgett¹, Rachel Steinhardt², Charles M. Brooks², Dennis Meier³, Darrell G. Schlom^{2,4,5}, David A. Muller^{1,4}, Julia A. Mundy^{1,6}

¹ School of Applied and Engineering Physics, Cornell University, Ithaca, New York 14853, USA

² Department of Materials Science and Engineering, Cornell University, Ithaca, New York 14853, USA

³ Department of Materials Science and Engineering, Norwegian University of Science and Technology, NTNU, 7491 Trondheim, Norway

⁴ Kavli Institute at Cornell for Nanoscale Science, Ithaca, New York 14853, USA

⁵ Leibniz-Institut für Kristallzüchtung, Max-Born-Str. 2, 12489 Berlin, Germany

⁶ Department of Physics, Harvard University, Cambridge, Massachusetts 02138 USA

We construct ferroelectric $(\text{LuFeO}_3)_m/(\text{LuFe}_2\text{O}_4)$ superlattices with varying index m to study the effect of confinement on topological defects. We observe a thickness-dependent transition from neutral to charged domain walls and the emergence of fractional vortices. In thin LuFeO_3 layers, the volume fraction of domain walls grows, lowering the symmetry from $P6_3cm$ to $P3c1$ before reaching the non-polar $P6_3/mmc$ state, analogous to the group-subgroup sequence observed at the high-temperature ferroelectric to paraelectric transition. Our study shows how dimensional confinement stabilizes textures beyond those in bulk ferroelectric systems.

Understanding transitions between a disordered and ordered phase was a major triumph of 20th century physics. In non-adiabatic transitions, the Kibble-Zurek framework describes a transition in which spontaneous symmetry breaking in disconnected regions creates topological defects [1,2]. While this model was developed in cosmology, it found application to a variety of solid-state systems, playing a central role in understanding phase transitions ranging from superfluid ⁴He and high-temperature superconductors. In particular, ferroelectric materials have topological defects such as vortices and domain walls, which have been used to study otherwise inaccessible topological phenomena in the same universality, answering cosmology-related questions [3–5]. The topological defects can be imaged at the micron scale with scanning probe or optical microscopy [6–9] or at the atomic-scale with transmission electron microscopy [10–13]. In addition to their significance for fundamental research, these vortices and domain walls exhibit emergent functional properties due to their unique electrostatics, representing nanoscale objects with distinct insulating, conducting, or magnetic properties that are not present in the homogeneous bulk phases [7,8,12,14–16].

Topologically rich structures in perovskite ferroelectric systems have recently been created and manipulated using geometric confinement to tune the interplay between strain and depolarization fields. Nanostructured systems such as ferroelectric disks, rods, and composites have displayed vortices, skyrmions, and waves [17–20]. Precise epitaxial growth can further generate new metastable phases hidden in the energy landscape and has been recently used to form ferroelectric/paraelectric superlattices that generate ferroelectric vortices [21] and polar skyrmions [22]. This opened the door to studying the chirality, negative capacitance, and piezoelectric responses in these topological structures [23–25]. These studies focused on “soft”

ferroelectrics, where the spontaneous polarization rotates from the direction it has in the bulk structure in response to geometric confinement.

Here, we present atomically-precise $(\text{LuFeO}_3)_m/(\text{LuFe}_2\text{O}_4)_1$ superlattices synthesized by reactive-oxide molecular beam epitaxy [26] as a unique synthetic construction to manipulate the existing topological textures in uniaxial ferroelectrics. Hexagonal LuFeO_3 is an improper ferroelectric that is isostructural to a class of materials including hexagonal manganites, gallates, indates, and tungsten bronzes. It has a robust ferroelectric polarization for temperatures up to 1020 K [27–30] and is a canted antiferromagnet below 147 K [31]. We layer LuFeO_3 with LuFe_2O_4 , which is epitaxially matched to LuFeO_3 but is non-polar in the bulk [32,33], and has a ferrimagnetic moment below 240 K [34], which in these $(\text{LuFeO}_3)_m/(\text{LuFe}_2\text{O}_4)_1$ superlattices creates a room-temperature multiferroic as previously reported [26]. In this work, we focus on the effect of confinement of the improper ferroelectric order using scanning transmission electron microscopy (STEM) to measure the polar displacements and the improper order parameter, [26,35] and map the domain walls and the underlying energy landscape. These measurements show that varying the thickness of LuFeO_3 changes the topological ordering and symmetries present in the system.

As shown in Fig. 1a, the improper ferroelectric polarization in LuFeO_3 is driven by a tilting of the iron-oxygen trigonal bipyramids which results in a polar “up-up-down” (+ P) or “down-down-up” (- P) displacement of the lutetium atoms [36,37]. The combination of the trimerization (breaking Z_3 symmetry) and polar distortion (breaking Z_2 symmetry) leads to a net Z_6 symmetry. The primary order parameter responsible for the symmetry breaking can be described by $\mathbf{Q} = (Q \cos \Phi, Q \sin \Phi)$ where Q is the amplitude of the distortion, and the phase Φ describes the in-plane displacements of the apical oxygens, which takes one of six discrete

values $\Phi_n = n\pi/3$, $n = 0, 1, \dots, 5$, in the polar $P6_3cm$ phase [13,28,38–40]. A lower symmetry state exists where the phase Φ varies continuously ($P3c1$), while the higher symmetry state with no distortions ($Q = 0$) gives the nonpolar $P6_3/mmc$ state [13,40]. The polarization arises due to a coupling to Q in the Landau free energy ($\sim Q^3 P \cos(3\Phi)$) [37,38,41].

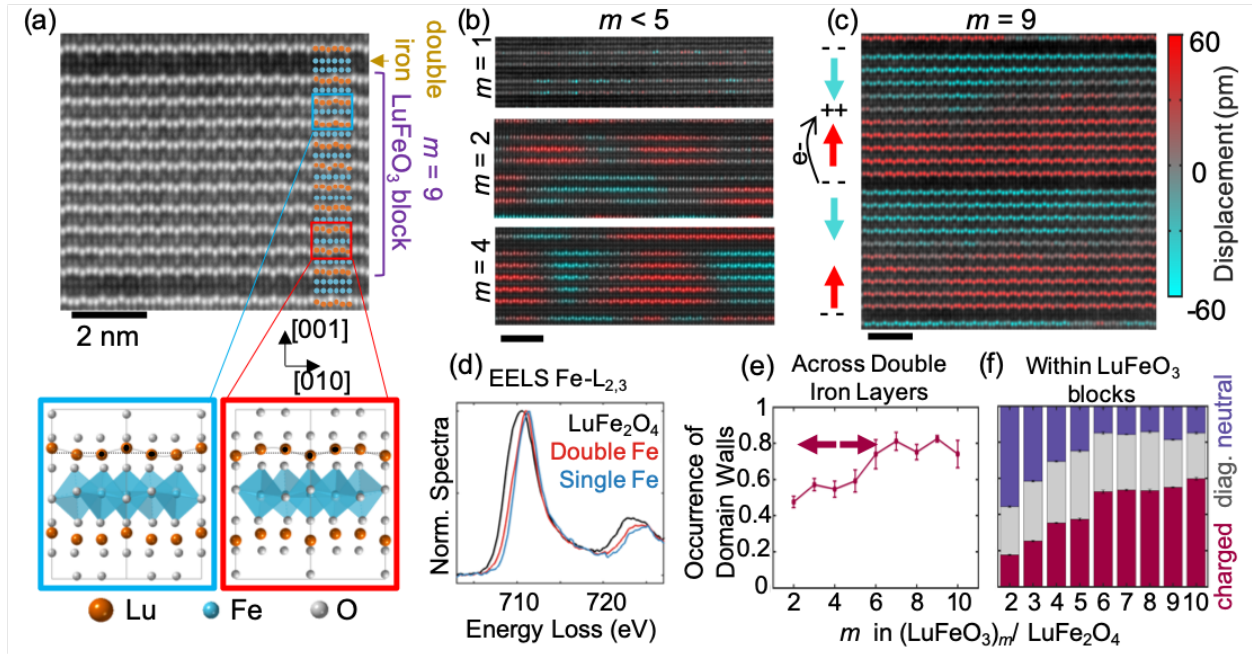


Figure 1. (a) HAADF-STEM image of an $m = 9$ $(\text{LuFeO}_3)_m/\text{LuFe}_2\text{O}_4$ superlattice, where bright (dark) contrast indicates lutetium (iron) atomic columns. Below is a cartoon of the crystal structure. A sinusoidal curve fits the lutetium displacements, giving the amplitude Q . The phase Φ , reflecting the in-plane apical oxygen rotations, can also be retrieved from the phase of the atomic displacements, as previously done in ref [12]. (b-d): Polarization color overlay, with cyan indicating polarization down and red indicating polarization up, for (b) $m = 1, 2$, and 4, and (c) $m = 9$, where head-to-head walls fall in the middle of the LuFeO_3 block. (d) EELS spectra of the Fe- $L_{2,3}$ edge of the double iron layers and single iron layers (the LuFeO_3 block) in an $m = 7$ superlattice compared to that of LuFe_2O_4 . (e) The fractional occurrence of the tail-to-tail configuration across the double iron layer, per in-plane distance along the double iron layer. (f) Fractional occurrence of neutral walls (angles $>60^\circ$ from horizontal), charged walls (angles $<30^\circ$), and diagonal walls ($30^\circ - 60^\circ$) within the LuFeO_3 block, per in-plane distance along the block.

Figure 1b-c shows the polarization as color overlays as the thickness, m , of the LuFeO_3 is increased (SI Fig. 1 shows P , Q , and Φ images). The index m corresponds to the number of formula-unit-thick LuFeO_3 layers in each repeat of the superlattice. Consistent with our previous report [26], we observe consistent polar distortions for $m \geq 2$ (Fig. 1b). The domains shown in

Fig. 1b for $m = 2, 4$ are small with a mixture of neutral and charged walls (larger field-of-view images are in SI Fig. 2). As the thickness of the LuFeO_3 layer is increased, the domain structure becomes more coherent. In the $m = 9$ sample in Fig. 1c, there are consistent polarization down domains at the top of the LuFeO_3 block, and polarization up domains at the bottom (larger field-of-view images are in SI Fig. 3). This pattern at high m enforces a tail-to-tail polarization configuration ($\leftarrow\rightarrow$) across the LuFe_2O_4 layer, and a head-to-head domain wall ($\rightarrow\leftarrow$) confined within the LuFeO_3 block.

Charged polarization configurations are typically energetically costly and only appear in bulk hexagonal manganites because of the topologically protected six-fold vortices. No vortices are observed that would prevent the material from only forming energetically favorable neutral walls, yet the charged head-to-head walls persist at high m , indicating that six-fold vortices are not imperative to form charged domain walls in this structure. Here we find the electrostatics of the superlattice play a critical role in stabilizing the domain walls. The double iron layers in the material nominally have an average iron valence of $2.5+$, compared to $3+$ in the LuFeO_3 block. Previously, density functional theory (DFT) results on this system have shown hole-doping of the double iron layer is energetically favorable, simultaneously creating a tail-to-tail polarization configuration which becomes increasingly stabilized with for larger m [26], as illustrated schematically in Fig. 1c. An electron energy loss spectroscopy (EELS) measurement of the iron valence (Fig. 1d and SI Fig 4) shows that in the double layers of the superlattice the iron valence is reduced slightly compared to the LuFeO_3 block, but remains higher than the $2.5+$ which is nominally observed in LuFe_2O_4 . This indicates hole doping in the double iron layer. The DFT combined with the EELS measurements indicate electrostatics in this confined system appear to generate the charged domain wall pattern.

We performed analysis of over 14,000 nm² (142,640 atomic columns) to generate robust statistics over $m = 1$ to 10. Consistent with the qualitative observations, the tail-to-tail polarization configuration is formed across most of the double iron layers (Fig. 1e), with increasing regularity for increasing m . The consequence is a propensity for head-to-head walls in the LuFeO₃ block, with higher regularity for higher m (SI Fig. 5). Further, charged head-to-head domain walls are stabilized in the thicker layers due to their unique electrostatics (Fig. 1f), becoming the dominant wall type for $m > 5$. As the confinement is increased, the size of the domains shrinks (with the in-plane length of the charged domain walls increasing linearly with m - SI Fig 5e), and the otherwise more energetically favorable neutral domain walls become relatively more prevalent for $m < 4$ (Fig. 1f).

This regular domain architecture is not observed in thin LuFeO₃ grown between paraelectric layers of InFeO₃ (SI Fig. 6) or in ultra-thin epitaxial films [42], which exhibit suppression of ferroelectric order due to clamping at the interface. Additionally, LuFeO₃ thin films grown on YSZ are monodomain (SI Fig. 6g-h and [30]), as are thin films of YMnO₃ [42]. In our work, no vortices have been observed in LuFeO₃ up to thicknesses of 200 nm, indicating that our superlattices with layers thinner than 6 nm are well under the critical thickness for spontaneous vortex formation. In this work, no lattice strain or depolarizing field is present between the LuFeO₃ and the LuFe₂O₄ to suppress ferroelectric order (SI Fig 7). The (LuFeO₃) _{m} /(LuFe₂O₄) synthetic construct thus provides us with an experimental system that stabilizes and confines charged domain walls, which is distinct from simply considering ultrathin ferroelectric layers.

Analysis of the STEM images allows us to measure the primary order parameter (Q , Φ) that drives the polarization configuration in the (LuFeO₃) _{m} /(LuFe₂O₄) superlattices [12]. Figure

2a shows the six trimerization domains corresponding to the Z_6 symmetry. The HAADF-STEM images are overlaid with the color scheme in Fig. 2 and 3, for larger and smaller m , respectively. Similar to bulk hexagonal manganites, we observe a phase change $\Delta\Phi = \pm \pi/3$ at domain walls within the LuFeO_3 blocks, for all walls within error in $m > 3$ and for $>90\%$ of walls for $m = 2, 3$ (SI Fig 5d) – the exceptions to this may be stabilized by the presence of defects in the weakly polar energy landscape. We do not observe a correlation of the phase across the LuFe_2O_4 beyond enforcing a tail-to-tail polarization configuration (SI Fig. 5c), so each LuFeO_3 block can be considered as an isolated, quasi-two-dimensional system of determined thickness.

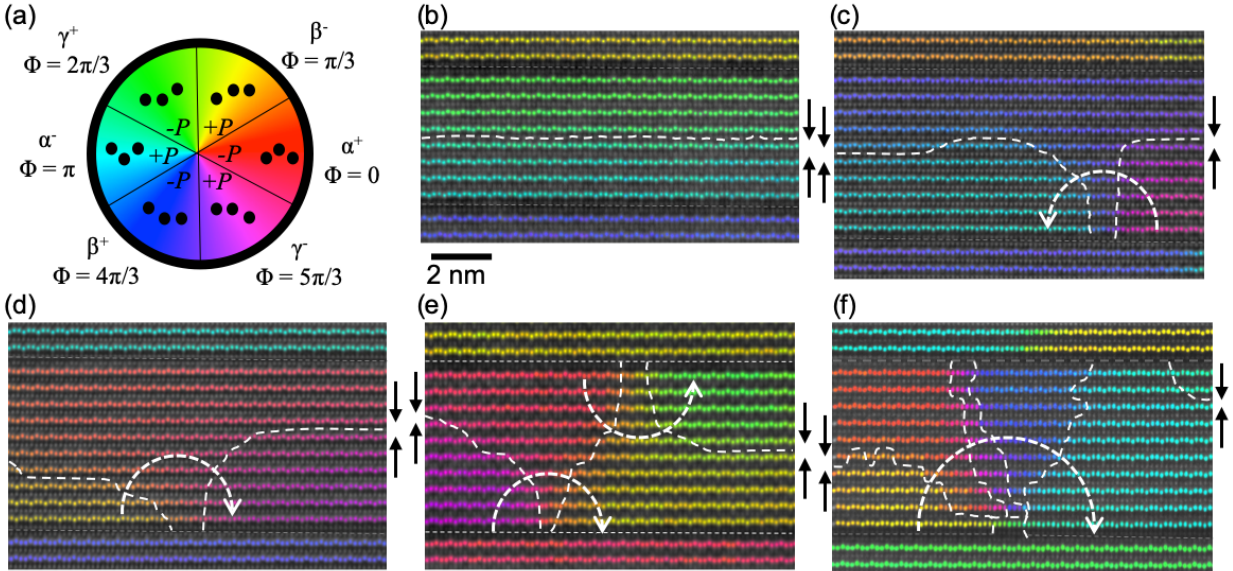


Figure 2. Φ overlay of STEM images showing the domain structure in $(\text{LuFeO}_3)_m/(\text{LuFe}_2\text{O}_4)$ superlattices for large m ($m = 7,9$). (a) Cartoon of the projection of lutetium positions for different Φ , with the color corresponding to the color overlays. (b) A stable charged domain wall, with black arrows showing polarization directions. (c-d) At the end of a domain in-plane, the phase rotates clockwise or anti-clockwise (white arrows), forming half vortices and anti-vortices to maintain the charged domain wall configuration. (e) For short in-plane domains, the phase can first wrap on one neighboring double iron layer and then the other. (f) Rarely, a vortex with five domains can be observed.

In our images of superlattices with $m > 4$, such as shown in Fig. 2, we observe “half-vortices” composed of three out of the six possible domain states sketched in Fig. 2a. The “core”

of such fractional vortices is pinned to the double iron layers as displayed in Fig. 2c-d. In Fig. 2e, two half-vortices appear side-by-side, with phases wrapping in the same direction. The systematic formation of such half-vortices in $(\text{LuFeO}_3)_m/(\text{LuFe}_2\text{O}_4)$ allows the system to stabilize head-to-head walls within the LuFeO_3 blocks, while keeping a tail-to-tail configuration across the LuFe_2O_4 layers. This behavior is fundamentally different from analogous bulk systems where the structural trimerization enforces six-fold vortices. While the splitting of structural vortices into “fragmented vortices” has been predicted to occur in systems away from the ground state [39], the observed correlation between preferred domain wall orientations and half-vortices is unexpected. Rarely, five domains come together at a point, shown in Fig. 2f, possibly stabilized by defects. The electrostatics which drive the tail-to-tail polarization configuration across the LuFe_2O_4 layer discourage or prohibit the formation of a full vortex – indeed, as noted above no bulk-like full vortices have been observed in this thin-film system for LuFeO_3 thicknesses up to 200 nm. Interestingly, as the phases wrap around the fractional vortices, they progress from Z_6 symmetry towards a $U(1)$ symmetry near the core (SI Fig. 8), analogous to the six-fold vortices in hexagonal manganites [12].

In the bulk case, the primary order parameter related to the structural symmetry breaking drives the formation of vortices, which enforce electrostatically unfavorable charged ferroelectric domain walls. In this system, the charged domain walls appear to co-determine the topological feature formation, favoring fractional vortices. The appearance of these “fractional” vortices suggests that the impact of electrostatics in the $(\text{LuFeO}_3)_m/\text{LuFe}_2\text{O}_4$ superlattices is a stronger influence than in the isostructural bulk system, softening the rigid hierarchy of energy scales.

In thinner layers, as the confinement of the LuFeO_3 layer is increased, small domains with neutral domain walls are increasingly prevalent. Images of the $m = 2$ and 4 structures are

shown in Fig. 3. For $m = 4$ in Fig. 3a, there are charged domain walls and fractional vortices, but also stripe patterns where the phase progresses across the in-plane direction of the sample, similar to states observed under strain in bulk crystals [43] but in this case, without strain. Tail-to-tail polarization orientation is not always enforced across the double iron layer. For $m = 2$ in Fig. 3b, we observe more instances of the topological stripe formation (with gradual phase winding, SI Fig. 9), although charged domain walls can also be found.

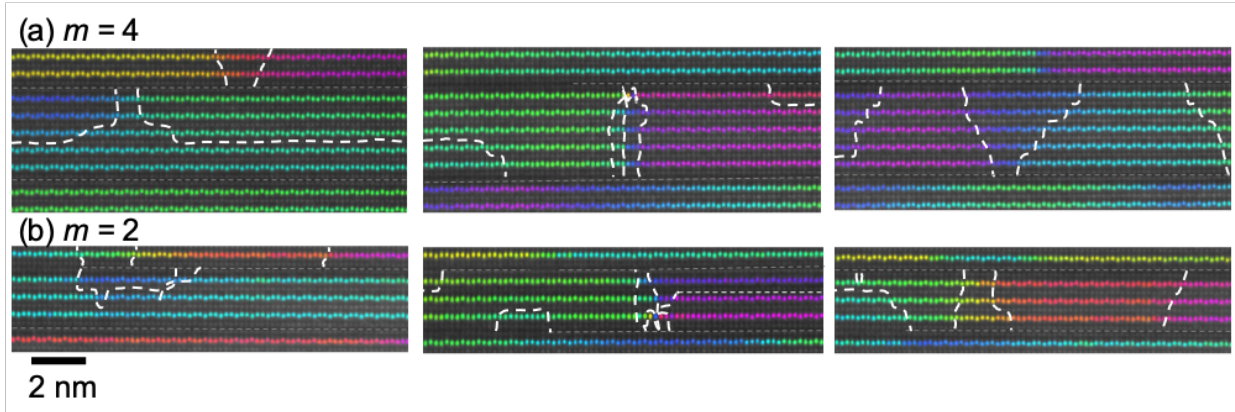


Figure 3. The order parameter Φ as a color overlay on the HAADF-STEM images for small m ($m = 4, 2$) where the neutral domain walls are observed with more equal occurrence. (a) for $m = 4$, we see a fairly equal co-existence of charged ferroelectric domain walls (left), and neutral + diagonal domain walls forming stripe patterns (right). We also see irregular numbers of domains coming together to a point in the middle image. (b) In the $m = 2$ case, we see smaller areas of charged domain walls (left) and more neutral walls forming in a stripe pattern (right). We also observe unusual numbers of domains intersecting (middle).

There is a resulting change to the global symmetry as the topological defects occupy an increasing fraction of the LuFeO_3 material with decreasing m . Figure 4a displays histograms of the logarithm of the occurrences of the structural order parameter, which maps the free energy landscape [12]. For $m \geq 4$, the domains have a well-defined energy landscape with six minima and Z_6 ($P6_3cm$) symmetry as expected. Here, intermediate states between the six wells corresponding to the domain walls. For $m = 1$, we observe the paraelectric state, corresponding to $P6_3/mmc$ symmetry. Interestingly, for $m = 2$, we observe a fairly uniform distribution of the structural

order parameter, which we might expect for a state with $P3c1$ symmetry, with values at low Q indicating some contribution from paraelectric states. Likewise, the $m = 3$ state shows slightly more weight in the ferroelectric wells, while also showing some contribution from paraelectric states. These distributions are integrated from many images and reflect the non-uniformity of the sample.

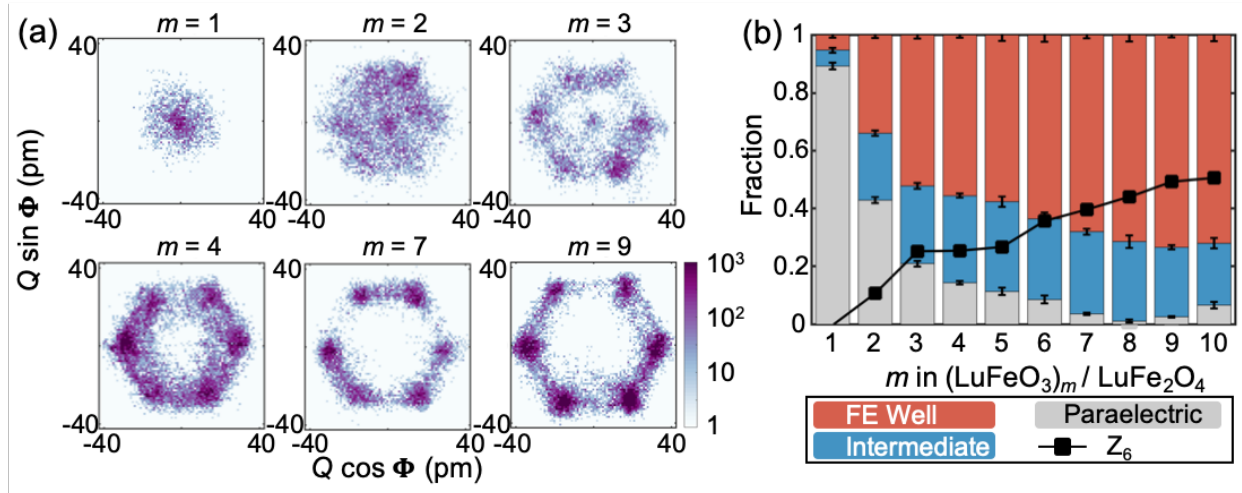


Figure 4. (a) Histograms of the order parameter for different m in $(\text{LuFeO}_3)_m/(\text{LuFe}_2\text{O}_4)$ superlattices, with the logarithm of the occurrences plotted. $m = 1$ shows a parabolic well, consistent with a paraelectric order parameter distribution. For $m = 2$ and 3, Q is slightly larger and the values of Φ are widely spread, indicating a combination of ferroelectric domain and intermediate Φ states. For $m = 4$, the six ferroelectric domains are visible while maintaining a large fraction of intermediate states. For $m = 7$ and 9, the six ferroelectric domains comprise the majority of the observed states, and the Q value is higher. (b) Relative amount of states in ferroelectric (FE) wells vs. in the intermediate states (between wells) vs. the paraelectric state. The difference between the states in the well and in the intermediate states tracks the relative amount of Z_6 symmetry.

As domain walls overlap within 2-3 nm of a vortex core in hexagonal ErMnO_3 , $U(1)$ symmetry emerges [12]. In these superlattices, the confinement length for $m = 2$ and 3 is similar to the domain wall width (SI Fig. 10), and the domain walls similarly overlap. For the $m = 2$ case, we observe local, atomic-scale polar distortions, but due to the abundance of domain walls, an overall $P3c1$ symmetry. This group-subgroup sequence is reminiscent of bulk ferroelectric transitions observed in YMnO_3 , where above the ferroelectric transition temperature, the average

structure is $P6_3/mmc$ symmetry, while pair distribution analysis suggests that there are local fluctuations that lower the local symmetry to $P3c1$ [40]. The important difference is that the transition in $(\text{LuFeO}_3)_m/\text{LuFe}_2\text{O}_4$ superlattices is driven by confinement and not by an increase in temperature as it is the case in YMnO_3 . The transition with confinement is quantified in Fig. 4b. We observe a cross-over in the dominant occupied states: the paraelectric state is dominant for $m = 1$; the paraelectric, ferroelectric well, and in-between well “intermediate” states are roughly balanced for $m = 2$; and the ferroelectric well states are most prevalent for $m > 3$.

In conclusion, we have demonstrated atomic-scale control of domain wall placement in the $(\text{LuFeO}_3)_m/(\text{LuFe}_2\text{O}_4)$ superlattice system, which further provides insight into the topology and symmetry of uniaxial ferroelectrics under dimensional confinement. In the thicker LuFeO_3 blocks, the topological defects consist largely of charged domain walls with “fractional” vortices pinned on the boundary LuFe_2O_4 layers—suggesting that the electrostatics imposed by the superlattice drive charged domain wall formation and the resulting three-fold vortices. This charged domain wall pattern is disrupted for thinner LuFeO_3 blocks, where smaller domains with neutral domain walls prevail. As the domain walls comprise more of the material, an emergent $P3c1$ symmetry is observed for $m = 2$ before becoming paraelectric for $m = 1$. We image this transition with atomic-scale resolution, observing both the local displacements and the average symmetry from sampling the overall energy landscape. This provides direct and simultaneous imaging of symmetry-lowering transition in confined LuFeO_3 layers. Moreover, as the vortex cores in these materials were previously associated with fractional electronic charge and quantized magnetic flux, highly confined vortex and fractional vortex states could display interesting physics and produce novel functionality.

Acknowledgements

We acknowledge discussions with Hena Das, Elizabeth Nowadnick, Craig Fennie, Sverre Selbach, Andres Cano, Sang-Wook Cheong, and Chris Nelson. We acknowledge technical support with the electron microscopy from Earl Kirkland, Malcolm Thomas, John Grazul and Mariena Silvestry Ramos. Research was supported by the US Department of Energy, Office of Basic Energy Sciences, Division of Materials Sciences and Engineering, under Award No. DE-SC0002334. The electron microscopy studies made use of the electron microscopy facility of the Cornell Center for Materials Research, a National Science Foundation (NSF) Materials Research Science and Engineering Centers program (DMR-1719875). DM was supported by NTNU via the Onsager Fellowship Program and the Outstanding Academic Fellows Program.

References

- [1] T. W. B. Kibble, *J. Phys. A: Math. Gen.* **9**, 1387 (1976).
- [2] W. H. Zurek, *Nature* **317**, 505 (1985).
- [3] S. M. Griffin, M. Lilienblum, K. T. Delaney, Y. Kumagai, M. Fiebig, and N. A. Spaldin, *Phys. Rev. X* **2**, 1 (2012).
- [4] S.-Z. Lin, X. Wang, Y. Kamiya, G.-W. Chern, F. Fan, D. Fan, B. Casas, Y. Liu, V. Kiryukhin, W. H. Zurek, C. D. Batista, and S.-W. Cheong, *Nat. Phys.* **10**, 970 (2014).
- [5] Q. N. Meier, M. Lilienblum, S. M. Griffin, K. Conder, E. Pomjakushina, Z. Yan, E. Bourret, D. Meier, F. Lichtenberg, E. K. H. Salje, N. A. Spaldin, M. Fiebig, and A. Cano, *Phys. Rev. X* **7**, 041014 (2017).
- [6] M. Fiebig, T. Lottermoser, D. Fröhlich, A. V. Goltsev, and R. V. Pisarev, *Nature* **419**, 818 (2002).
- [7] T. Choi, Y. Horibe, H. T. Yi, Y. J. Choi, W. Wu, and S.-W. Cheong, *Nat. Mater.* **9**, 253 (2010).
- [8] D. Meier, J. Seidel, A. Cano, K. Delaney, Y. Kumagai, M. Mostovoy, N. A. Spaldin, R. Ramesh, and M. Fiebig, *Nat. Mater.* **11**, 284 (2012).
- [9] W. Wu, Y. Horibe, N. Lee, S.-W. Cheong, and J. R. Guest, *Phys. Rev. Lett.* **108**, 077203 (2012).
- [10] Q. H. Zhang, L. J. Wang, X. K. Wei, R. C. Yu, L. Gu, A. Hirata, M. W. Chen, C. Q. Jin, Y. Yao, Y. G. Wang, and X. F. Duan, *Phys. Rev. B - Condens. Matter Mater. Phys.* **85**, 2 (2012).
- [11] T. Matsumoto, R. Ishikawa, T. Tohei, H. Kimura, Q. Yao, H. Zhao, X. Wang, D. Chen, Z. Cheng, N. Shibata, and Y. Ikuhara, *Nano Lett.* **13**, 4594 (2013).
- [12] M. E. Holtz, K. Shapovalov, J. A. Mundy, C. S. Chang, Z. Yan, E. Bourret, D. A. Muller, D. Meier, and A. Cano, *Nano Lett.* **17**, 5883 (2017).
- [13] F.-T. Huang, X. Wang, S. M. Griffin, Y. Kumagai, O. Gindele, M.-W. Chu, Y. Horibe, N. A. Spaldin, and S.-W. Cheong, *Phys. Rev. Lett.* **113**, 267602 (2014).
- [14] Y. Geng, N. Lee, Y. J. Choi, S. W. Cheong, and W. Wu, *Nano Lett.* **12**, 6055 (2012).
- [15] J. A. Mundy, J. Schaab, Y. Kumagai, A. Cano, M. Stengel, I. P. Krug, D. M. Gottlob, H. Doğanay, M. E. Holtz, R. Held, Z. Yan, E. Bourret, C. M. Schneider, D. G. Schlom, D. A. Muller, R. Ramesh, N. A. Spaldin, and D. Meier, *Nat. Mater.* **16**, 622 (2017).
- [16] D. Meier, *J. Phys. Condens. Matter* **27**, 463003 (2015).
- [17] Z. Liu, B. Yang, W. Cao, E. Fohtung, and T. Lookman, *Phys. Rev. Appl.* **8**, 034014

- (2017).
- [18] Y. Nahas, S. Prokhorenko, L. Louis, Z. Gui, I. Kornev, and L. Bellaiche, *Nat. Commun.* **6**, 1 (2015).
 - [19] I. I. Naumov, L. Bellaiche, and H. Fu, *Nature* **432**, 737 (2004).
 - [20] A. Schilling, D. Byrne, G. Catalan, K. G. Webber, Y. A. Genenko, G. S. Wu, J. F. Scott, and J. M. Gregg, *Nano Lett.* **9**, 3359 (2009).
 - [21] A. K. Yadav, C. T. Nelson, S. L. Hsu, Z. Hong, J. D. Clarkson, C. M. Schlepütz, A. R. Damodaran, P. Shafer, E. Arenholz, L. R. Dedon, D. Chen, A. Vishwanath, A. M. Minor, L. Q. Chen, J. F. Scott, L. W. Martin, R. Ramesh, C. M. Schlepütz, A. R. Damodaran, P. Shafer, E. Arenholz, L. R. Dedon, D. Chen, A. Vishwanath, A. M. Minor, L. Q. Chen, J. F. Scott, L. W. Martin, and R. Ramesh, *Nature* **530**, 198 (2016).
 - [22] S. Das, Y. L. Tang, Z. Hong, M. A. P. Gonçalves, M. R. McCarter, C. Klewe, K. X. Nguyen, F. Gómez-Ortiz, P. Shafer, E. Arenholz, V. A. Stoica, S. L. Hsu, B. Wang, C. Ophus, J. F. Liu, C. T. Nelson, S. Saremi, B. Prasad, A. B. Mei, D. G. Schlom, J. Íñiguez, P. García-Fernández, D. A. Muller, L. Q. Chen, J. Junquera, L. W. Martin, and R. Ramesh, *Nature* **568**, 368 (2019).
 - [23] A. R. Damodaran, J. D. Clarkson, Z. Hong, H. Liu, A. K. Yadav, C. T. Nelson, S.-L. Hsu, M. R. McCarter, K.-D. Park, V. Kravtsov, A. Farhan, Y. Dong, Z. Cai, H. Zhou, P. Aguado-Puente, P. García-Fernández, J. Íñiguez, J. Junquera, A. Scholl, M. B. Raschke, L.-Q. Chen, D. D. Fong, R. Ramesh, and L. W. Martin, *Nat. Mater.* **16**, 1003 (2017).
 - [24] P. Shafer, P. García-Fernández, P. Aguado-Puente, A. R. Damodaran, A. K. Yadav, C. T. Nelson, S.-L. Hsu, J. C. Wojdeł, J. Íñiguez, L. W. Martin, E. Arenholz, J. Junquera, and R. Ramesh, *Proc. Natl. Acad. Sci.* **115**, 915 (2018).
 - [25] A. K. Yadav, K. X. Nguyen, Z. Hong, P. García-Fernández, P. Aguado-Puente, C. T. Nelson, S. Das, B. Prasad, D. Kwon, S. Cheema, A. I. Khan, C. Hu, J. Íñiguez, J. Junquera, L. Q. Chen, D. A. Muller, R. Ramesh, and S. Salahuddin, *Nature* **565**, 468 (2019).
 - [26] J. A. Mundy, C. M. Brooks, M. E. Holtz, J. A. Moyer, H. Das, A. F. Rébola, J. T. Heron, J. D. Clarkson, S. M. Disseler, Z. Liu, A. Farhan, R. Held, R. Hovden, E. Padgett, Q. Mao, H. Paik, R. Misra, L. F. Kourkoutis, E. Arenholz, A. Scholl, J. A. Borchers, W. D. Ratcliff, R. Ramesh, C. J. Fennie, P. Schiffer, D. A. Muller, and D. G. Schlom, *Nature* **537**, 523 (2016).
 - [27] E. Magome, C. Moriyoshi, Y. Kuroiwa, A. Masuno, and H. Inoue, *Jpn. J. Appl. Phys.* **49**, 09ME06 (2010).
 - [28] H. Das, A. L. Wysocki, Y. Geng, W. Wu, and C. J. Fennie, *Nat. Commun.* **5**, 2998 (2014).
 - [29] W. Wang, J. Zhao, W. Wang, Z. Gai, N. Balke, M. Chi, H. N. Lee, W. Tian, L. Zhu, X. Cheng, D. J. Keavney, J. Yi, T. Z. Ward, P. C. Snijders, H. M. Christen, W. Wu, J. Shen, and X. Xu, *Phys. Rev. Lett.* **110**, 1 (2012).
 - [30] S. M. Disseler, J. A. Borchers, C. M. Brooks, J. A. Mundy, J. A. Moyer, D. A. Hillsberry, E. L. Thies, D. A. Tenne, J. Heron, M. E. Holtz, J. D. Clarkson, G. M. Stiehl, P. Schiffer, D. A. Muller, D. G. Schlom, and W. D. Ratcliff, *Phys. Rev. Lett.* **114**, 217602 (2015).
 - [31] J. A. Moyer, R. Misra, J. A. Mundy, C. M. Brooks, J. T. Heron, D. A. Muller, D. G. Schlom, and P. Schiffer, *APL Mater.* **2**, 012106 (2014).
 - [32] D. Niermann, F. Waschkowski, J. de Groot, M. Angst, and J. Hemberger, *Phys. Rev. Lett.* **109**, 16405 (2012).
 - [33] S. Lafuerza, J. García, G. Subías, J. Blasco, K. Conder, and E. Pomjakushina, *Phys. Rev.*

- B **88**, 85130 (2013).
- [34] A. D. Christianson, M. D. Lumsden, M. Angst, Z. Yamani, W. Tian, R. Jin, E. A. Payzant, S. E. Nagler, B. C. Sales, and D. Mandrus, *Phys. Rev. Lett.* **100**, 107601 (2008).
 - [35] L. Li, P. Gao, C. T. Nelson, J. R. Jokisaari, Y. Zhang, S. J. Kim, A. Melville, C. Adamo, D. G. Schlom, and X. Pan, *Nano Lett.* **13**, 5218 (2013).
 - [36] B. B. Van Aken, T. T. M. Palstra, A. Filippetti, and N. A. Spaldin, *Nat. Mater.* **3**, 164 (2004).
 - [37] C. J. Fennie and K. M. Rabe, *Phys. Rev. B - Condens. Matter Mater. Phys.* **72**, 1 (2005).
 - [38] S. Artyukhin, K. T. Delaney, N. A. Spaldin, and M. Mostovoy, *Nat. Mater.* **13**, 42 (2014).
 - [39] M. Lilienblum, T. Lottermoser, S. Manz, S. M. Selbach, A. Cano, and M. Fiebig, *Nat. Phys.* **11**, 1070 (2015).
 - [40] S. H. Skjærvø, Q. N. Meier, M. Feygenson, N. A. Spaldin, S. J. L. Billinge, E. S. Bozin, and S. M. Selbach, *Phys. Rev. X* **9**, 31001 (2019).
 - [41] A. Cano, *Phys. Rev. B - Condens. Matter Mater. Phys.* **89**, 214107 (2014).
 - [42] J. Nordlander, M. Campanini, M. D. Rossell, R. Erni, Q. N. Meier, A. Cano, N. A. Spaldin, M. Fiebig, and M. Trassin, *Nat. Commun.* **10**, 5591 (2019).
 - [43] X. Wang, M. Mostovoy, M. G. Han, Y. Horibe, T. Aoki, Y. Zhu, and S.-W. Cheong, *Phys. Rev. Lett.* **112**, 247601 (2014).